Bulletin of Volcanology (2021) 83:2
https://doi.org/10.1007/s00445-020-01425-0

RESEARCH ARTICLE

Tsunamis from prospected mass failure on the Marsili submarine volcano flanks and hints for tsunami hazard evaluation

G. Gallotti[1] · F. Zaniboni[1] · G. Pagnoni[1] · C. Romagnoli[2] · F. Gamberi[3] · M. Marani[3] · S. Tinti[1]

Received: 19 September 2020 / Accepted: 30 November 2020

Abstract

The Marsili Seamount (Tyrrhenian Sea, Italy) is the largest submarine volcano in the Mediterranean Sea, located in the middle of the Marsili Basin, facing the Calabrian and Sicilian coasts on its eastern side, and the coasts of Sardinia on the opposite side. It has erupted in historical times, and its summit crest is affected by widespread hydrothermal activity. This study looks at mass failures taking place at different depths on the flanks of the volcano and estimates their associated tsunamigenic potential. Mass failure, tsunami generation, and propagation have been simulated by means of numerical models developed by the Tsunami Research Team of the University of Bologna. In all, we consider five cases. Of these, three scenarios, one regarding a very small detachment and two medium-sized ones (between 2 and 3 km^3 failure volume), have been suggested as possible failure occurrences in the published literature on a morphological basis and involve the north-eastern and north-western sectors of the volcano. The two additional cases, one medium-sized and one extreme, intended as a possible worst-case scenario (volume 17.6 km^3), affecting the eastern flank. Results indicate that small-volume failures are not able to produce significant tsunamis; medium-size failures can produce tsunamis which dangerously affect the coasts if their detachment occurs in shallow water, i.e., involves the volcano crest; and extreme volume failures have the potential to create disastrous tsunamis. In all the simulations, tsunami waves appear to reach the Aeolian Islands in around 10 min and the coasts of Calabria and Sicily in 20 min. This study highlights that there is a potential for dangerous tsunamis generation from collapses of the Marsili volcano and as a consequence a need to intensify research on its status and stability conditions. More broadly, this investigation should also be extended to the other volcanic seamounts of the Tyrrhenian Sea, since their eruptive style, evolution, and tsunamigenic potential are still poorly known.

Keywords Marsili volcano · Landslide tsunamis · Tyrrhenian seamounts · Tsunami hazard

Introduction

Submarine mass movements have been widely investigated in literature (e.g., Vanneste et al. 2006; Homa 2009; Alves 2015), often with a focus on assessing the related tsunamigenic potential, which is mainly achieved by means of numerical methods (Harbitz 1992; Pelinovsky and Poplavsky 1996; Tinti and Piatanesi 1997; Tinti et al. 1999; Satake 2001; Ward 2001; Ward and Day 2001; Dutykh and Dias 2009; Gallotti et al. 2020). In particular, flank instability commonly affects submarine and insular volcanoes, because of slope oversteepening and of loading enhanced by eruptive or seismic activity (e.g., Satake 2001; Tinti et al. 2006; Loughlin et al. 2010; Sassa et al. 2016; Walter et al. 2019). Further, magma intrusion and strong hydrothermalism have proved to be factors favoring slope instability on volcanoes, due to their effect on pore-fluid pressure (McGuire 1996; Reid 2004).

The most voluminous volcanic flank collapse in historic times (Ritter Island, Papua New Guinea, 1888) and many other cases (see, e.g., the series of Krakatau events from 1883 to the recent 22nd December 2018) have shown that

Editorial responsibility: W. W. Chadwick, Jr.; acting Executive Editor L. Pioli

✉ G. Gallotti
glauco.gallotti2@unibo.it

[1] Department of Physics and Astronomy (DIFA), University of Bologna, Bologna, Italy

[2] Department of Biological, Geological, and Environmental Sciences (BIGEA), University of Bologna, Bologna, Italy

[3] Institute of Marine Sciences, National Research Council (ISMAR-CNR), Bologna, Italy

Published online: 08 December 2020

they can produce tsunamis with catastrophic effects in the nearby ocean basins (see Giachetti et al. 2012; Karstens et al. 2019; Grilli et al. 2019). Together with the Oshima-Oshima and Mt. Unzen (Japan) events of 1741 and 1792, respectively, these collapses caused more than 15,000 casualties (Siebert et al. 1987; Begét 2000; Auker et al. 2013; Day 2015). Collapses on the flanks of volcanic islands or submarine volcanoes may involve larger volumes than on subaerial volcanoes (Watt et al. 2014; Hunt et al. 2018) and constitute an important threat that is unfortunately underrated in the natural hazard mitigation policies for many of the involved countries.

Reconstructing pre-historical and historical gravity instability occurrences and building scenarios of potential future events require specific analyses of the geological and morphological characteristics of the site under study, information not always available for deep water areas.

Regardless of landslide magnitude and source, the following three stages can be distinguished in the evolution of mass failure and related tsunamis: slope failure (I), landslide evolution (II), and tsunami generation and propagation (III). At the onset of stage I, when the slope stability is lost, the slide starts moving. During the sliding process (stage II), some landslides evolve into debris flows and turbidity currents, whereas others (slides or slumps) maintain a more coherent behavior with limited internal deformations (Locat and Lee 2002). By interacting with water, the slide generates water waves (stage III), which propagate outwards. While stages II and III are usually viewed as dynamic processes, the conventional analysis of slope failure (stage I) commonly focuses on the final limit-equilibrium state, which is a static condition (e.g., Paparo and Tinti 2017).

In this work, we consider five potential scenarios of mass failures: four cases affecting the north-eastern and eastern flank and one on the north-western side of the Marsili Seamount (MS), an active (Iezzi et al. 2014; Tamburrino et al. 2015) submarine volcano located in the southern Tyrrhenian Sea, Italy, and evaluate the related tsunamigenic potential. Volcanic eruptions may represent a direct threat themselves, but, since the MS vents are deep in the sea, the formation of eruptive columns above the sea surface capable of affecting the coasts seems an unlikely occurrence. The main potential hazard of MS is related to the fact that eruptions, possibly in connection with seismic activity, might trigger mass movements that, in turn, might induce tsunami waves.

The aims of this study are (1) to reconstruct three past landslide events with volumes up to 2.8 km^3 occurred on the MS based on the available literature (see next sections for details) and estimate their tsunamigenic potential; (2) to simulate two further possible failures on the MS, with volumes of 2.4 km^3 and 17.6 km^3, the latter being intended as a worst-case scenario; and (3) to study the landslide-tsunami propagation pattern in the southern Tyrrhenian Sea from the MS source area.

Geological setting

The MS is the largest submarine volcano in Europe, located in the southern part of the Tyrrhenian Sea (Fig. 1), about 120 km north of Sicily and 170 km west of Calabria. It is considered to be the axial, super-inflated spreading ridge of the Marsili back-arc basin (Marani and Trua 2002; Cocchi et al. 2009; Trua et al. 2018), and was mostly built in the last 1–0.7 Myr through eruptions from central and fissural vents (Iezzi et al. 2014). Its eruptive products record the flow of asthenospheric mantle into the mantle wedge induced by the lateral tearing of the subducting Ionian slab (Marani and Trua 2002). The resulting increase of melt supply favored the vertical accretion of the Marsili volcano (Marani 2004).

The edifice is a NNE-SSW-elongated seamount rising over 3000 m from the basin floor to a minimum sea depth of 500 m. It has a length of ~ 70 km and a mean width of 20 km, with steep flanks (Figs. 2 and 3, left panel). The bulk volume of the volcano edifice is about 3000 km^3 (Ventura et al. 2013). The MS summit crest zone (25 km long), approximately bounded by the 1000-m contour, shows narrow linear alignments of volcanic ridges and cones (Marani and Trua 2002; Ventura et al. 2013) with diameters up to 200–300 m (Ligi et al. 2014). The axial rift is the principal site of stress release, marking the preferential trend of dyke emplacement along the spreading center (Marani 2004). Hydrothermal activity is widespread along the rift zone (Ligi et al. 2014), where the occurrence of more recent explosive eruptive activity (last 7 kyr) has been suggested by Iezzi et al. (2014) and Tamburrino et al. (2015). OBS monitoring on the Marsili summit recorded volcanic tremor events and seismic sequences indicative of geothermal fluid circulation and/or magma movements attributable to the persistent, present-day volcanic activity (D'Alessandro et al. 2009).

Linear volcanic structures (vents alignments) along the tip regions of the volcano continue down to the basin floor (Fig. 2). Circular, small-size volcanic edifices are widespread on the western flank of the seamount (Fig. 3, left panel) that is undergoing constructional volcanic processes (Ventura et al. 2013). On the contrary, a smoother seafloor characterizes the eastern flank of the volcano due to sediment coverage and to mass wasting at a variety of scales. This sector of the MS is said to lie above the magma chamber (Trua et al. 2002). The occurrence of a shallow magmatic reservoir (about 2000 m below the MS summit) is, in fact, proposed on the basis of magnetic and gravity data (Caratori Tontini et al. 2010). A progressive steepening of the flanks of the volcano takes place from its basal to its summit regions and, in the upper part of the edifice, slope angles exceeding 30° (Fig. 2). The summit

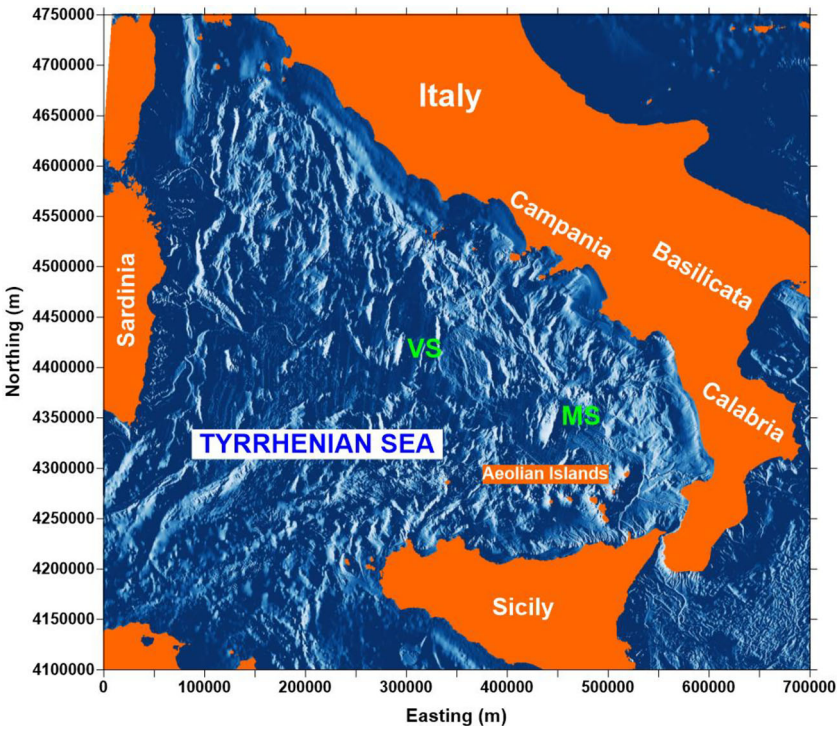

Fig. 1 Tyrrhenian Sea bathymetry (from the EMODnet database 2018) and surrounding land showing the location of the Marsili Seamount (MS) and Vavilov Seamount (VS). Coordinates are in UTM-WGS84 projection, zone 33N

part of the seamount is a narrow, relatively flat area and corresponds to a region with low density and low magnetic anomalies, likely indicative of extensive hydrothermal alteration (Caratori Tontini et al. 2010). Steep escarpments, mainly with a NNE-SSW trend, are present on both flanks of the edifice (Fig. 2; Ventura et al. 2013) and may contribute to structurally controlled volcano flank instability. In the north-eastern and north-western sectors of the seamount, morphological evidences of past collapses are indicated by Caratori Tontini et al. (2010) and Ventura et al. (2013) although, according to the latter authors, unequivocal evidence of large-scale sector/flank collapses is lacking.

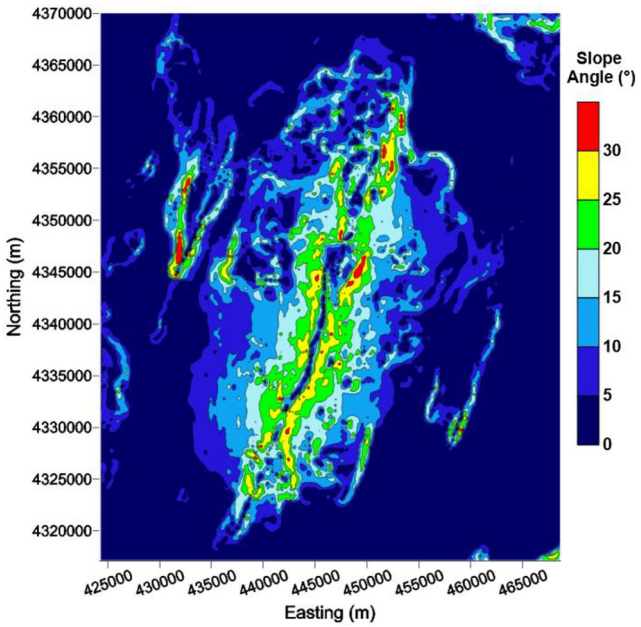

Fig. 2 Slope map of the Marsili Seamount. See Fig. 1 for location

Methods and data

In this study, three collapses are reconstructed based on evidence proposed in literature (Caratori Tontini et al. 2010; Ventura et al. 2013). In addition, two hypothesized scenarios are simulated for the south-eastern flank of the MS. In Fig. 3, the reconstructed initial sliding areas and the respective bathymetric profiles passing through the slide's center of mass are plotted on the present-day morphology. Table 1 summarizes the main associated geometrical features, sizes, and estimated runout.

The mass failure scenarios denoted by (a), (b), and (c) are justified by present-day evidence:

(a) This is the only site where a fan-like body and displaced blocks have been detected at the foot of the MS flank in deep water, attributable to a past slide (Ventura et al. 2013). We have tentatively located the detachment area for this simulated case between 800 and 1400 m depth (Fig. 3a).

(b) This deep section of the north-eastern volcano flank (between 2400 and 3200 m; Fig. 3b) has been previously suggested as a possible source area of a past medium-size collapse (Caratori Tontini et al. 2010). Despite the lack of an evident deposit at its foot, the steep slopes and

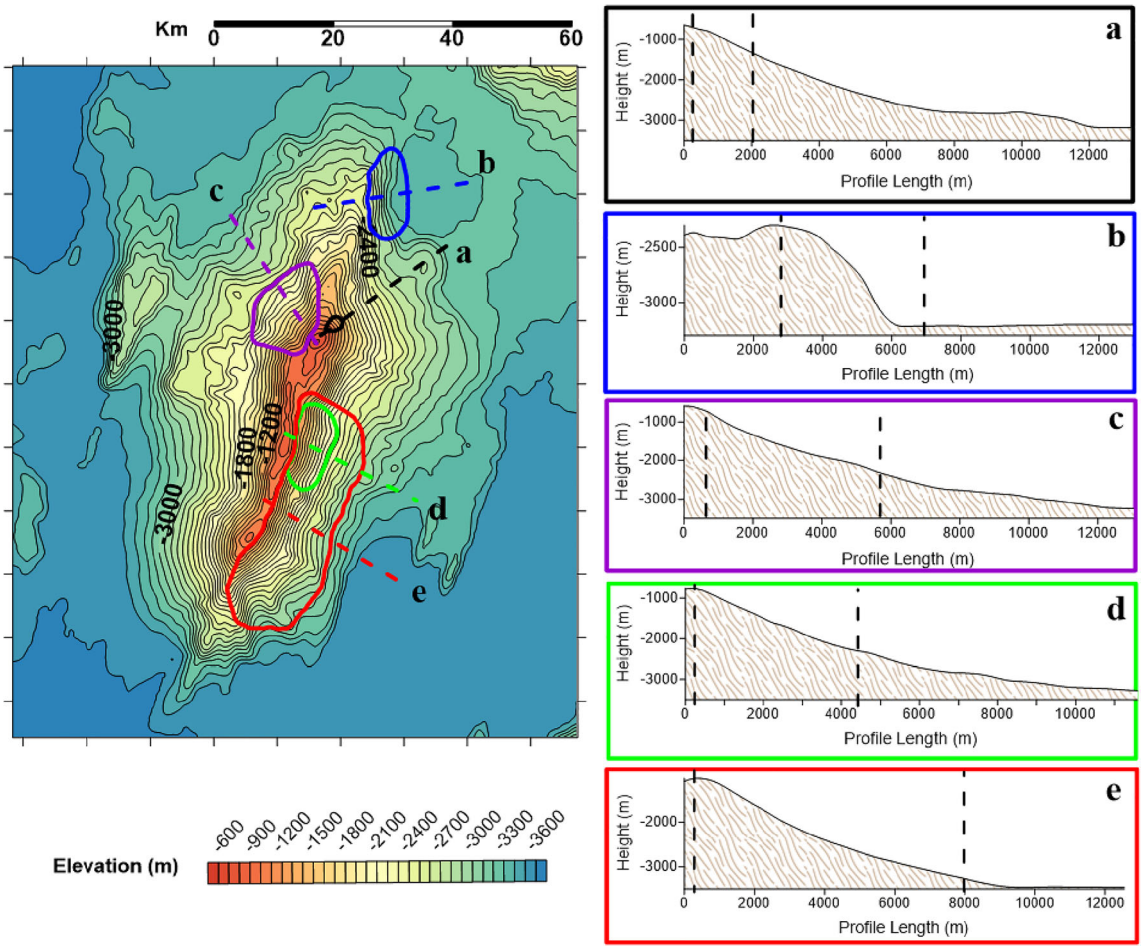

Fig. 3 Left panel: location of the considered mass failure source areas (full colored lines), in different colors, and related bathymetric transects. Right panel: cross sections along the transects according to the present-day morphology. The dashed lines delimit the initial sliding areas assumed for each studied case. Cases (a), (b), and (c) are considered as previous events, while cases (d) and (e) are hypothetical, the latter representing the worst-case scenario

the evident asymmetry between the eastern and western flank of the MS in this area provide robust hints of a deep-seated failure occurrence affecting this sector in the past.

(c) The area of the north-western flank located between 800 and 2300 m depth (Fig. 3c) has been suggested by Caratori Tontini et al. 2010 as the source of a past collapse. A scar morphology, open to the north-west, is recognizable in this sector, embracing a wide portion of the volcano flank

The following cases designated by (d) and (e) are fully hypothetical and represent instability events potentially affecting the volcanic edifice along the central-southern, narrow

Table 1 Synthetic data of all the mass failure simulations

Case	Volume (km^3)	Minimum scar depth (m)	Average initial thickness (m)	Maximum initial thickness (m)	Slide duration (s)	Velocity peak (m/s)	Average deposit thickness (m)	Runout (km)
Past events								
(a)	0.04	− 800	28	70	280	52	23	8.5
(b)	2.8	− 2400	180	415	140	25	160	2
(c)	2.7	− 800	100	245	310	60	90	12
Hypothesized scenarios								
(d)	2.4	− 1000	140	350	280	65	137	10
(e)	17.6	− 900	160	450	290	65	140	4.5

summit part, characterized by high slope values (Figs. 2 and 3). They are introduced for the sake of completeness and involve medium to large volumes of rocks detaching from the crest. Specifically:

(d) This hypothetical failure is located just below the summit (between 1000 and 2200 m depth; Fig. 3d), where, in case of an eruption, the development of gravity instability is more probable, owing to steep slopes (larger than 25°) and the weakness of the crest rocks enhanced by hydrothermal alteration (Caratori Tontini et al. 2010).
(e) This hypothetical failure involves a large portion of the central-southern summit and of the eastern MS flank between 900 and 2900 m depth (Fig. 3d). It is designed to estimate the largest tsunamis expected from a large-scale failure potentially affecting this sector of the MS. Flank collapses of this size cannot be ruled out in volcanoes presenting elongated structures and steep slopes like the MS and the nearby Vavilov Seamount (Fig. 1; see also Caratori Tontini et al. 2010).

Thickness and volumes of the past sliding masses (Table 1 and Fig. 4) are reconstructed following different criteria. For case (a), an average initial thickness of 28 m and a volume of 0.04 km^3 are considered. For case (b), a volume of 2.8 km^3 is assumed by considering the "mass deficit" of the eastern flank with respect to the western one. Specifically, the MS shows a general bilateral symmetry that is partially interrupted in this sector (Fig. 3), potentially suggesting a displaced (initial) mass as thick as 180 m on average, by comparison with the opposite, less steep flank. Similarly, in case (c), a volume of 2.7 km^3 is reconstructed considering the scar geometry with respect to an originally (i.e., "pre-failure") regular morphology. For cases (d) and (e), the initial mass failure thickness is fully hypothesized on geometrical basis as 140 m and 160 m and involves estimated volumes of 2.4 km^3 and 17.6 km^3, respectively (Table 1). Cross sections of the assumed slide geometry are shown in Fig. 4 only for the past cases supported by morphological evidence, i.e., cases (a), (b), and (c).

The motion of the landslides has been computed by means of the model UBO-BLOCK2 (see e.g., Tinti et al. 1997; Lo Iacono et al. 2012; Zaniboni and Tinti 2019). It discretizes the total mass into a matrix of interacting blocks that are allowed to change shape, preserving volume, and that cannot separate from one another. The model requires that the size of the constituent blocks is smaller than the scale of the main morphological features of the sliding surface. Their motion is mainly controlled by the gravity force and by the resistance acting on the bottom and front surfaces of the blocks, namely the basal friction and the water drag. Moreover, the model requires the specification of the bottom friction and frontal drag coefficients which are set based on previous studies on other tsunamigenic systems in the Tyrrhenian Sea (see Zaniboni et al. 2016).

The sliding mass, moving on the seabed, perturbs the sea level, generating a train of positive and negative oscillations that propagate all over the basin. The computation of the tsunamigenic impulse, namely of the vertical displacement of the water surface due to the motion of the sliding body, is performed through the application of the numerical code UBO-TSUIMP. This accounts for the change of water depth in each point of the tsunami computational grid due to the passage of the slide, filtering components with a spatial scale smaller than the local sea depth, and results in a tsunamigenic forcing lasting until the landslide comes to a rest. This is very different from the tsunamigenic forcing due to earthquakes, which in most cases is assumed as an instantaneous process (Synolakis 2003).

The simulation of the tsunami propagation is carried out by solving the Navier-Stokes equations in the shallow water equations (SWEs) approximation (Sadourny 1975). This approximation is known to neglect wave dispersion and therefore to overestimate the amplitude of the leading front of the tsunami. This effect however is of little importance for tsunamis generated by large and subcritical submarine landslides (Harbitz et al. 2006) as the ones dealt with in this paper. The equations are solved by means of a finite-difference method, based on a leap-frog scheme with a staggered-grid technique. This is implemented by the code UBO-TSUFD in its linear and non-linear versions, which is capable of treating systems of nested grids at an arbitrary level of nesting with full two-way information transmission between any pair of coupled grids. On the external open boundaries, the code applies conditions of pure transparency. On coastal boundaries, one option is a pure wave reflection assuming the existence of a rigid fixed vertical wall. A further option is a moving boundary technique, separating dynamically dry and wet regions, which enables one to compute tsunami land inundation. This numerical procedure (originally described in Tinti and Tonini 2013) has been applied with success to many cases of earthquake as well as landslide tsunamis, such as in Zaniboni et al. (2013), Zaniboni et al. (2014), Pagnoni et al. (2015), Loreto et al. (2017), Zaniboni and Tinti (2019), and Gallotti et al. (2020).

The SWEs are solved on regularly spaced grids by the UBO-TSUFD code. Since we want to explore the impact of mass failures on the peri-Tyrrhenian coasts, we built a mesh (grid 1) embracing almost the entire basin, made of over 450,000 nodes, covering an area of 591 × 432 km^2, with a 750-m-space resolution (see the red box in Fig. 5). The region closer to the MS is included in grid 2 (blue box in Fig. 5) that is formed by more than 700,000, 250-m-spaced, nodes, over an area of 214 × 216 km^2. In the source region, to better characterize the tsunamigenic forcing due to the slides, we built an even finer grid (grid 3, in green, Fig. 5) centered on the MS with 50-m-node spacing. It extends over 42 × 58 km^2, counting about 1 million total nodes.

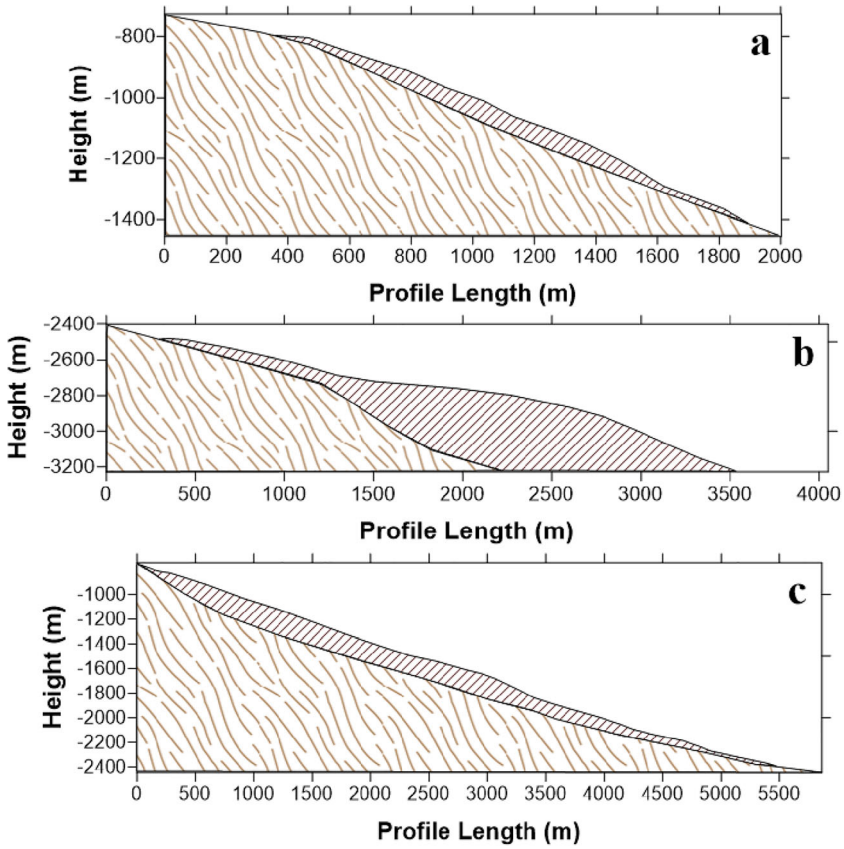

Fig. 4 Initial sliding masses (shown as areas with oblique pattern) considered for cases (a), (b), and (c): their basal surface coincides with the present-day morphology, their upper surface with a pre-slide morphology. These cross sections are portions of the profiles shown in Fig. 3 (right panel, delimited by the dashed black lines). Note differences in scales

Grids 1 and 2 are handled as a system of two nested grids, with grid 1 nested within grid 2, and information passed both ways through the common boundary at any time step. The technique foresees that in the region common to both grids, tsunami waves are computed only in the innermost grid (grid 1) and that tsunami computations are performed in all grids at the same time. As regards the larger domain (grid 3), we used a different approach. Here, we initialized the tsunami calculations providing the elevation and the horizontal momentum fields computed at a given time T1 after the slide onset. In practice, we computed the tsunami from the initial time up to T1 in the system of grids 1 and 2; then, we extracted the fields at time T1 and passed them to grid 3 to compute the tsunami evolution for all times following T1. For all simulations, we found it convenient to adopt T1 = 4 min.

The bathymetry data used to create all the meshes for slide and tsunami simulations come from the EMODnet database (2018). It has a ~ 160-m resolution and it is shown in Fig. 5 as a shaded relief.

Results

Past events

The results of cases from (a) to (c) are given in Fig. 6 and the related quantitative data are summarized in Table 1 for all the simulations. In case (a) (Fig. 6a), the sliding mass is partitioned into 15 blocks. The slide follows a SW-NE trajectory, running down a 9-km-long path in about 280 s, and stops close to a sub-rounded morphological high of likely eruptive origin. The computed average thickness of the slide deposit is slightly lower than the initial slide thickness, 23 m vs. 28 m. The peak velocity of 52 m/s is reached after 70 s. In case (b) (Fig. 6b), the sliding mass is partitioned into 51 regular blocks. The slide moves downslope, stopping some 2 km away from the detachment scar, after it reaches the wide flat area at its foot. The computed slide deposit thickness is slightly reduced with respect to its initial value during the motion, which lasts for only 140 s, and shows a velocity peak of 25 m/s after 80 s. In case (c) (Fig. 6c), the slide is partitioned into 106 blocks. The path that is about 12 km long is covered in 310 s. The 60 m/s velocity peak is reached after 80 s and maintained for about 30 s. The final slide deposit is roughly 10 m lower than the initial average thickness of 100 m. Note that, due to the considerable depths and velocity ranges, all the slide motions are in a subcritical regime (i.e., Froude number lower than 1).

The maximum water elevation of the tsunamis generated by the (a), (b), and (c) landslide scenarios is illustrated in Fig. 7 for the respective source areas, covered by the highest resolution domain (grid 3, see Fig. 5). It should be noted that scenarios (a) (the smallest landslide) and (b) (medium-volume source in deeper water) produce negligible initial waves compared to (c) (medium-volume source in shallower water).

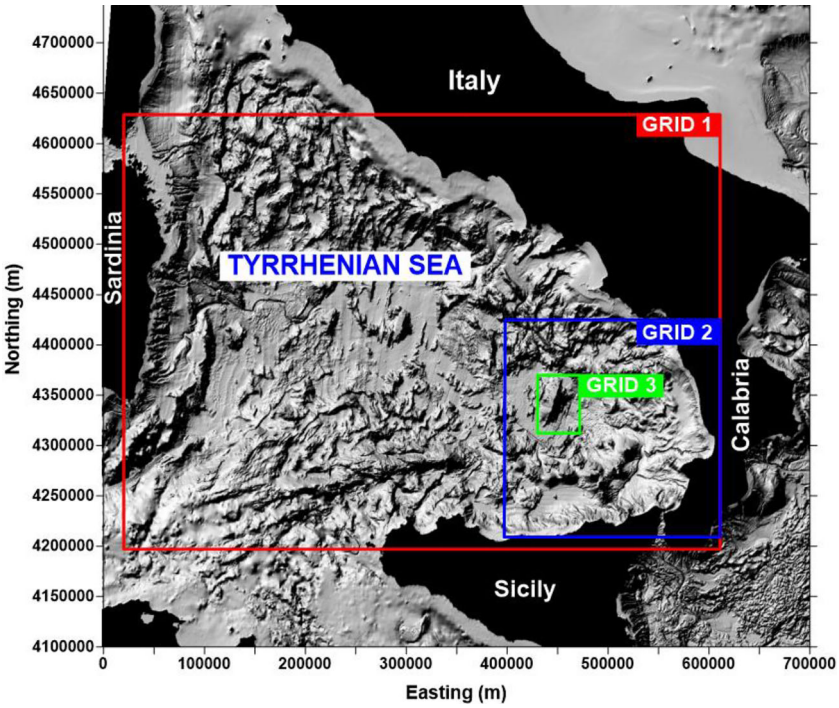

Fig. 5 Computational grid system for the tsunami simulations. In the largest domain (grid 1) cell size is 750 × 750 m. Grid 2 cell size is 250 × 250 m and grid 3, which is centered on the source area with a 50-m-space resolution, forms a nested-grid system. Coordinates are in UTM-WGS84 projection, zone 33N

For case (a), the water elevation of the generated tsunami is less than 1 cm, and for case (b), it is only a few centimeters. This suggests that scenarios of this kind do not produce tsunamis that are relevant to natural hazards. Conversely, in case (c), the water elevation is in the order of meters. This suggests the generation of a remarkable tsunami, as can be seen in the propagation shots over the smaller grid in Fig. 8. The typical landslide-tsunami pattern, which consists of an almost circular wavefront radiating from a point-like source, can be seen in the first frames, with the sign of the leading wave changing: positive leading waves (in yellow to red-magenta) move westwards while a negative leading front (in cyan-blue) moves in the opposite direction. The waves reach the surrounding coasts in about 20–30 min. Elevation along the coasts is shown in Fig. 9. Maximum values of 3–4 m can be found in the southern Campania region. Calabria and Sicily coasts show lower values, in the order of 2–3 m, and still lower values of 0.5–1 m are obtained for Sardinia.

Hypothesized scenarios

In case (d) (Fig. 10d), the slide is partitioned into 57 regular blocks and reaches the basin floor in about 280 s. The 65 m/s velocity peak is attained after 100 s at a depth of 2700 m. In the last case (e) (Fig. 10e), the hypothesized landslide body is partitioned into 85 blocks. The CoM trajectory follows a NW-SE path along the main slope gradient. The flank collapses rapidly: in slightly less than 5 min (290 s), the whole modelled mass moves from the seamount flank and spreads out over the basin. In the final position, the originally regular simulated mass distribution is partially lost. The final area is broader, resulting in a lower average thickness of 140 m of the slide mass vs. the initial one of 160 m. The CoM velocity reaches a peak of 65 m/s at $t = 105$ s, like in case (c). Nevertheless, some individual blocks reach velocity values as high as 80 m/s.

The propagation of the tsunami possibly generated by these scenarios over the intermediate grid 2 (see Fig. 5) is shown in Fig. 11. Both scenarios have in common a positive leading wave (red-magenta) moving eastward, and a negative one (cyan-blue) travelling in the opposite direction.

In both simulations, the northern Aeolian Islands are affected by the waves after 10 min and the interaction with the shallower bathymetry starts deforming the wavefront, as the result of refraction processes. The northern Sicily and Calabria coasts are hit by the tsunami some 20 min after the slide onset time: the 20-min sketches show a leading front almost parallel to the coast, with a main positive crest followed by a strong trough. Notice also the reflected waves, at $t = 15$ min in the Aeolian area and at $t = 30$ min for the Calabrian coast. Indeed, the only relevant difference between the two propagation patterns is the order of magnitude.

Enlarging further the investigation domain (grid 1 in Fig. 5), Figs. 12 and 13 show the maximum computed water elevations at the coast and the travel time map for scenarios (d) and (e), respectively. The highest waves affect the coasts of south Campania and north Calabria and the short coastal stretch of Basilicata, at a distance of approximately 200 km: for scenario (d), this portion is hit by waves at least 1 m high (in yellow, Fig. 12), with peaks of 3 m in Campania and Basilicata (red, Fig. 12); for scenario (e), in the same area, at

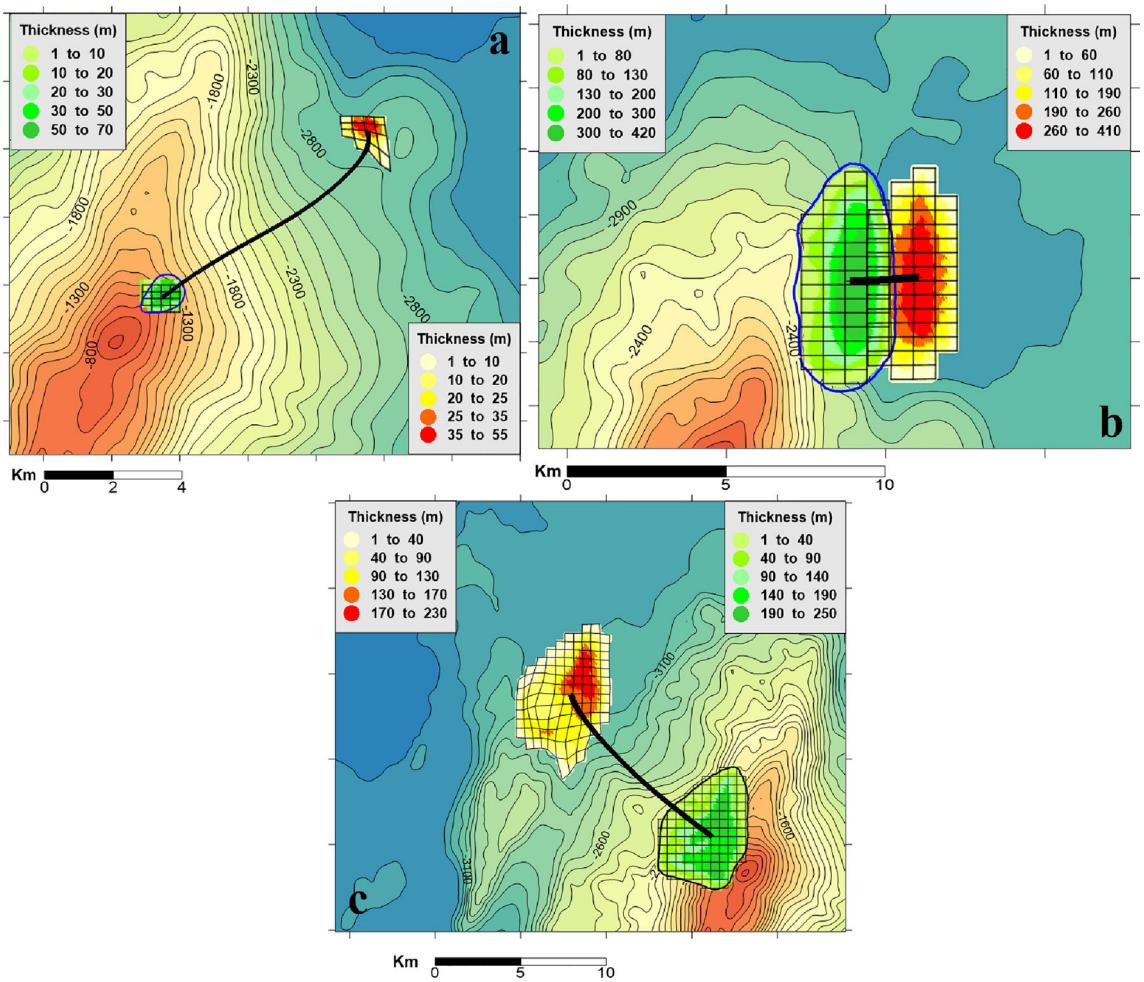

Fig. 6 Initial and final positions and trajectories of the modeled mass failures for the cases (a), (b), and (c). The initial and final thicknesses (in meters) are shown with light green-green and yellow-red palettes, respectively (note the different scales). Block partitions are shown in light black. The black lines denote the slides CoM trajectories. Bathymetric contouring is every 100 m

least 5-m maximum waves are predicted (in orange, Fig. 13), with extreme values exceeding 20 m in Basilicata and 15 m in southern Campania and north Calabria. Focusing on the Sicily coasts, one can see that they are partially protected by the Aeolian Islands, as stated above. However, for scenario (e), waves from 5 to 10 m affect the coast. The computational domain extends also to Sardinia, about 400 km west of the MS. For case (d) (Fig. 12), the hazard can be considered moderate here (with wave elevation less than half a meter), whereas, for case (e), elevations from 2 to 4 m are expected (Fig. 13).

Other interesting information contained in Figs. 12 and 13 concerns the tsunami travel times. In both simulated cases, the most affected areas, namely south Campania, Basilicata, and north Calabria, are reached in about 20 min. The same holds for Sicily. The tsunami travels faster towards the west, where it propagates in deeper water, and reaches Sardinia in about 45 min, with an average velocity close to 600 km/h, manifesting as a water retreat (as inferred from the negative front heading westward in the propagation sketches of Fig. 11). Notice that the travel times for the two scenarios (with volumes differing by one order of magnitude) mainly coincide, since they mainly depend on the basin bathymetry.

Discussion

In this work, we have modelled three landslide events believed to have occurred on the flanks of the MS (southern Tyrrhenian Sea, Italy). Current evidences allow the definition of most likely source areas conveniently and estimation of possible geometries and volumes of mass failures, but do not give information on the timing of the specific event. Actually, observations of widespread mass wasting deposits are lacking in the case of MS, since the present bathymetry of the surrounding Marsili Basin is very regular and smooth.

This study aims to disclose the consequences of these past submarine mass failures in terms of tsunami generation. For the sake of completeness, two other hypothetical cases of mass failure (one representing a worst-case scenario) are also simulated. In these instances, the considered initial sliding

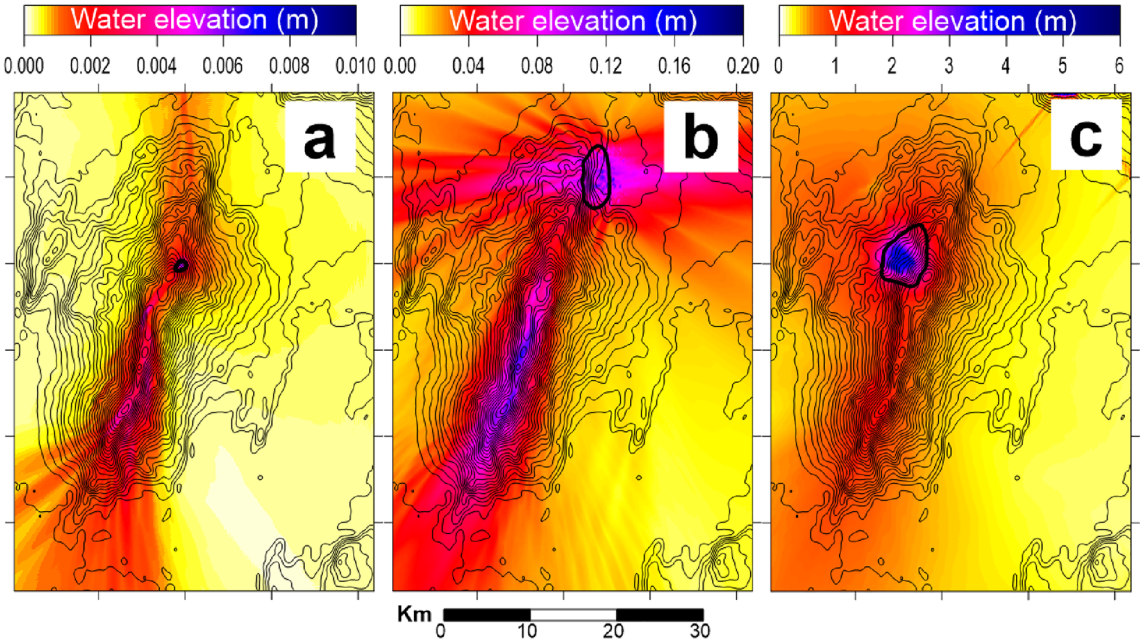

Fig. 7 Maximum water elevation over each node of the computational grid 3, covering the source area for scenarios (a), (b), and (c). The black lines contour the source areas of each scenario. Note the different scale of the color palette

areas and hypothesized masses are mainly based on geomorphological considerations, but not on direct evidences. The study cases allow to (1) evaluate how the volume and location of the possible mass movement on the volcano flank might influence the tsunami propagation and (2) analyze the possible effect of larger events in terms of tsunami hazard.

Our study makes use of a scenario-based technique. Adopting a different approach (e.g., probabilistic) is very difficult due to the lack of information limits our ability to better constrain the future events and their likelihood. The approach we followed in this paper has been applied to other volcanoes and proved to be an efficient method for tsunami hazard evaluation (e.g., Boudon et al. 2007; Waythomas et al. 2009; Karstens et al. 2019).

All the mass failures simulations do not show substantial deformations during the motion. This is due to the way the model computes the movement and the blocks' interactions. Nevertheless, it has been proved that the slide's deformation does

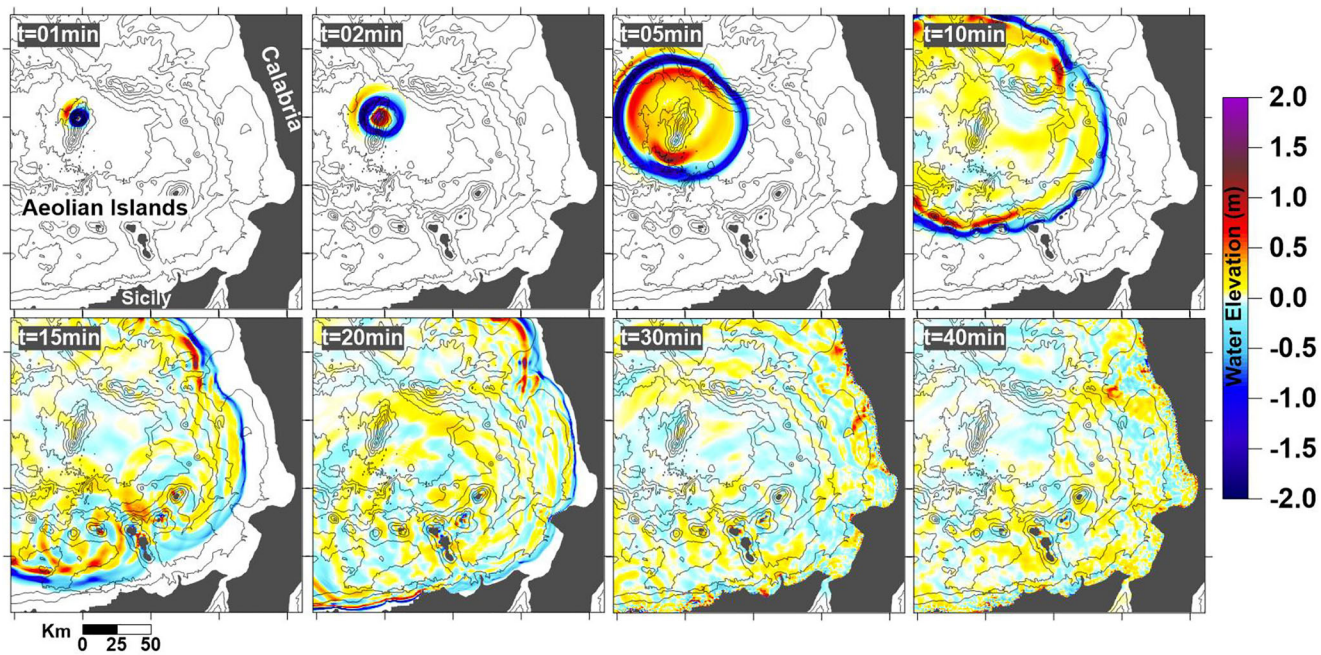

Fig. 8 Propagation of the tsunami generated by the hypothesized failure of case (c) over the intermediate domain, grid 2

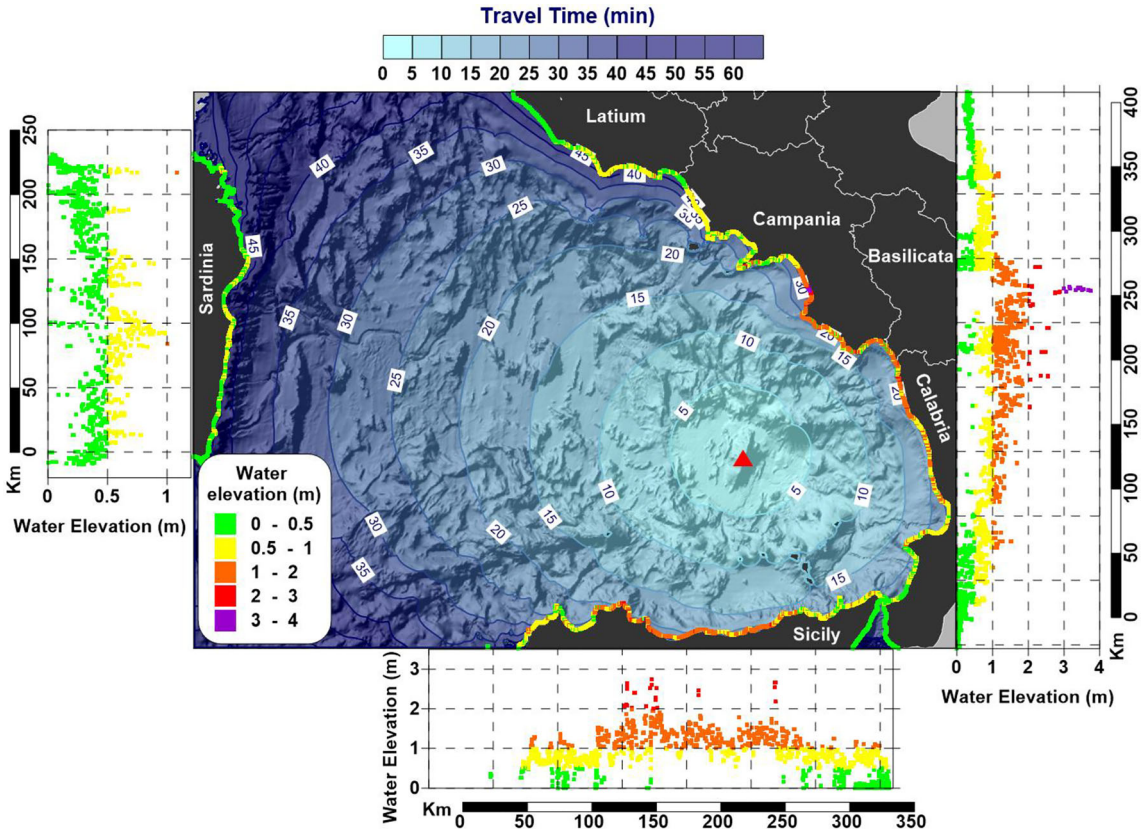

Fig. 9 Central panel: maximum water elevation associated with the passage of the tsunami along the coasts of the Tyrrhenian Sea, computed for the landslide scenario (c) (grid 1). Travel times (in minutes) are marked by the blue contouring. Left panel: maximum water elevation along the coast of Sardinia. Bottom panel: maximum water elevation along the northern Sicily coast. Right panel: maximum water elevation measured along the Tyrrhenian coasts of the Italy mainland. The red triangle denotes the MS

not influence the tsunami generation considerably (Løvholt et al. 2015) unless the slide evolves rapidly to a turbidity current. For mass failures occurred in the past, we have reproduced a relatively small-scale movement (a) based on evidence of slide deposits (blocks) found in the area by Ventura et al. (2013), and two medium-size failures (b)–(c) at different depths, following the evidence proposed by Caratori Tontini et al. (2010).

A relevant finding is that cases (a) and (b) do not generate noticeable tsunami waves. Hence, small-scale movements or medium-size failures in deep waters do not produce relevant tsunamis propagating in surrounding areas. Thus, the influence of mass failures geometry and depth on the tsunami generation is apparent (see Grilli and Watts 2005 for experimental validations), whereas case (c), due to the kind of motion and depth of movement, is able to generate waves as high as 4 m. At present, evidence of tsunami waves of this magnitude has not been found in the peri-Tyrrhenian coasts, probably because of the low preservation potential of tsunami-related features and

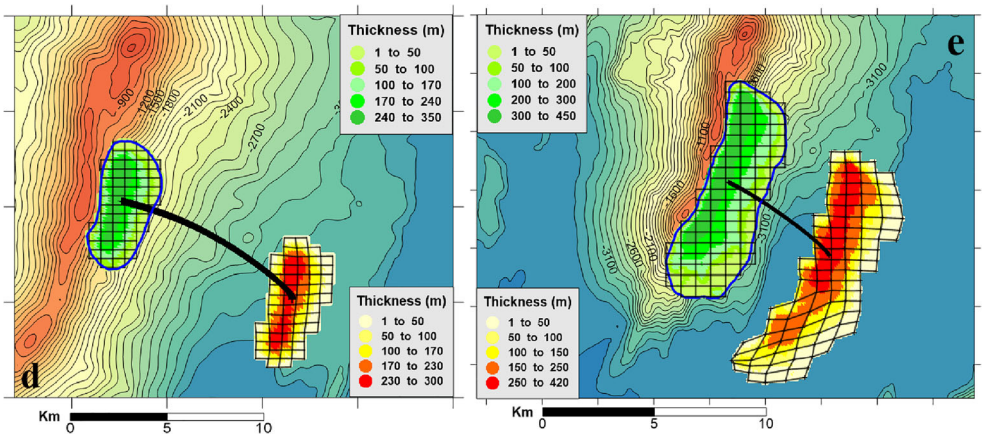

Fig. 10 Initial and final positions and trajectories of the modeled mass failures for the hypothesized (cases (d) and (e)). See caption of Fig. 6 for details

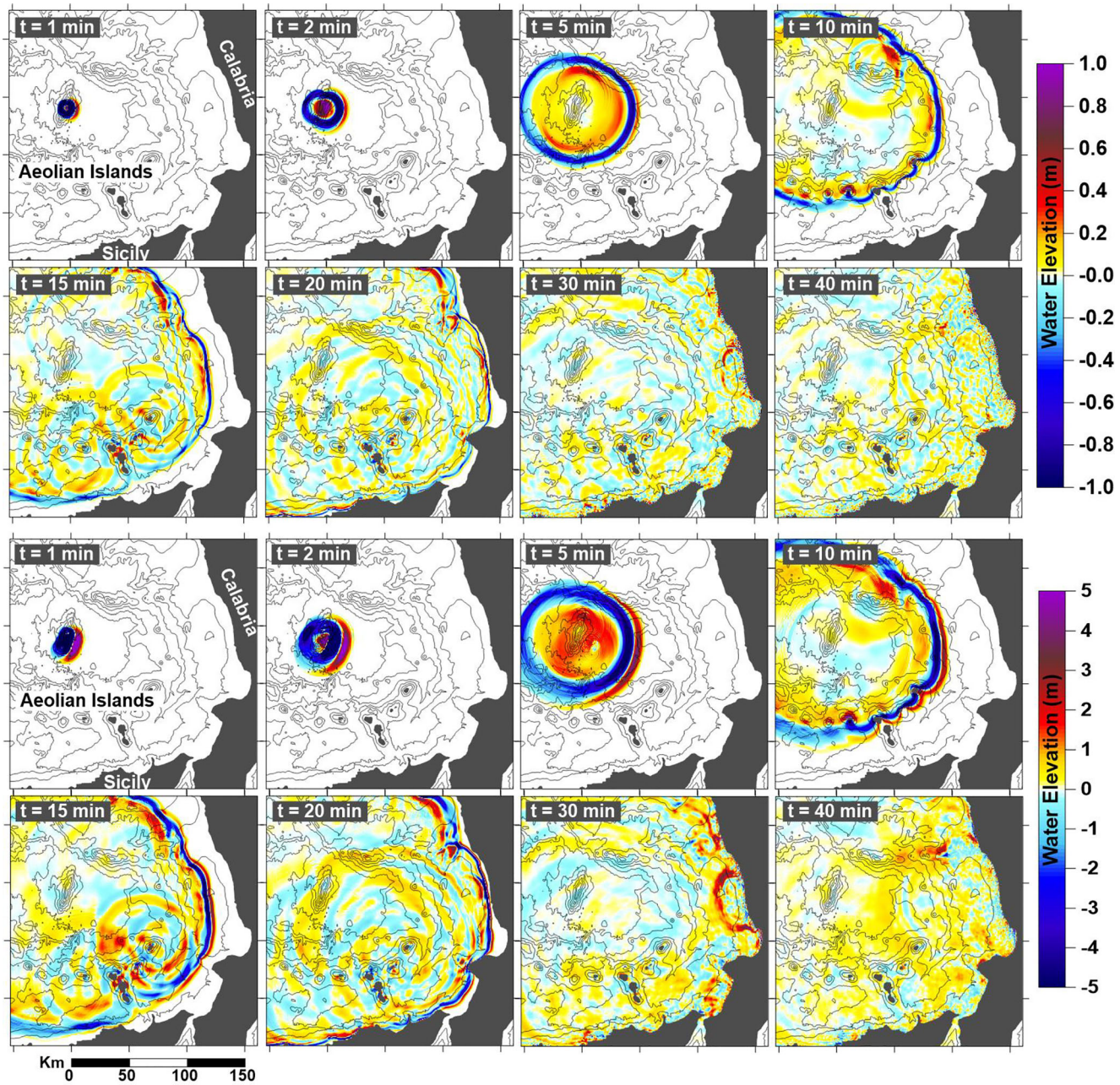

Fig. 11 Maximum tsunami elevation for the hypothesized cases (d) and (e) (left and right graphs, respectively) over grid 2. The black boundaries mark the border of the initial sliding body. The color palette is saturated at 10 m. Coordinates are in UTM-WGS84 projection, zone 33N

deposits and the lack of specific surveys. Furthermore, the scar associated with case (c) could be the result of different failure events that might have occurred at different times, resulting in multiple, smaller-scale, or negligible tsunamis.

The two hypothesized scenarios account for a 2.8-km^3 scar close to the sea surface (case (d)), located just below a narrow and steep segment of the volcano summit, and a wide flank/sector collapse of 17.6 km^3 of the south-eastern flank (case (e)). The hypothesized source for case (d) is close to the numerous vents that cover a large part of the volcano crest. In the presence of strong volcanic or seismic activity, these steep areas could be destabilized, also because of the low-density and fragile rocks forming the summit crest (Caratori Tontini et al. 2010). Case (e) has been hypothesized by considering the analogy between the MS and the Vavilov seamount. This latter is located some 170 km north-west of the MS (Fig. 1) and exhibits a morphology that can be interpreted as the result of a huge sector collapse affecting its western flank (Caratori Tontini et al. 2006). Due to the strong asymmetry between the eastern and the western flanks, the Vavilov edifice has been speculated, in fact, to have been affected by a massive sector collapse (Marani and Gamberi 2004; Caratori Tontini et al. 2010). Since Marsili and Vavilov

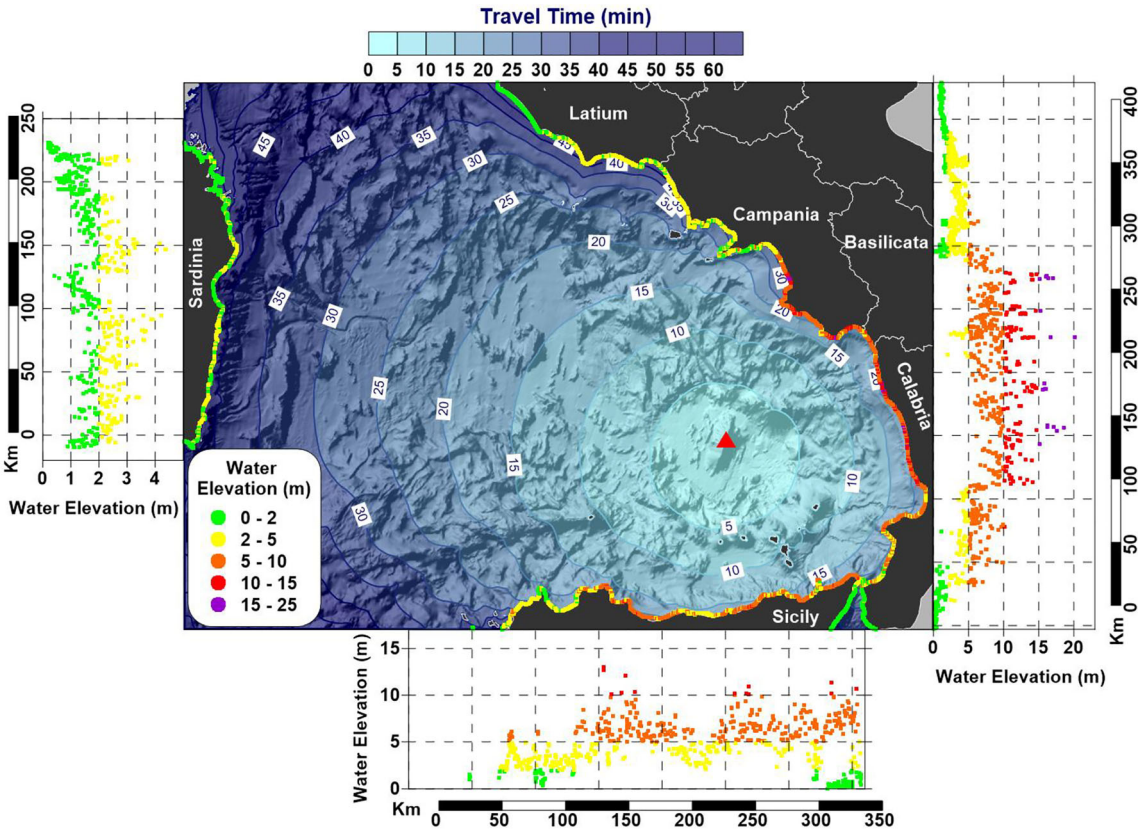

Fig. 12 Maximum water elevation along the coasts of the Tyrrhenian Sea, computed for the landslide case (d). See caption of Fig. 9 for details

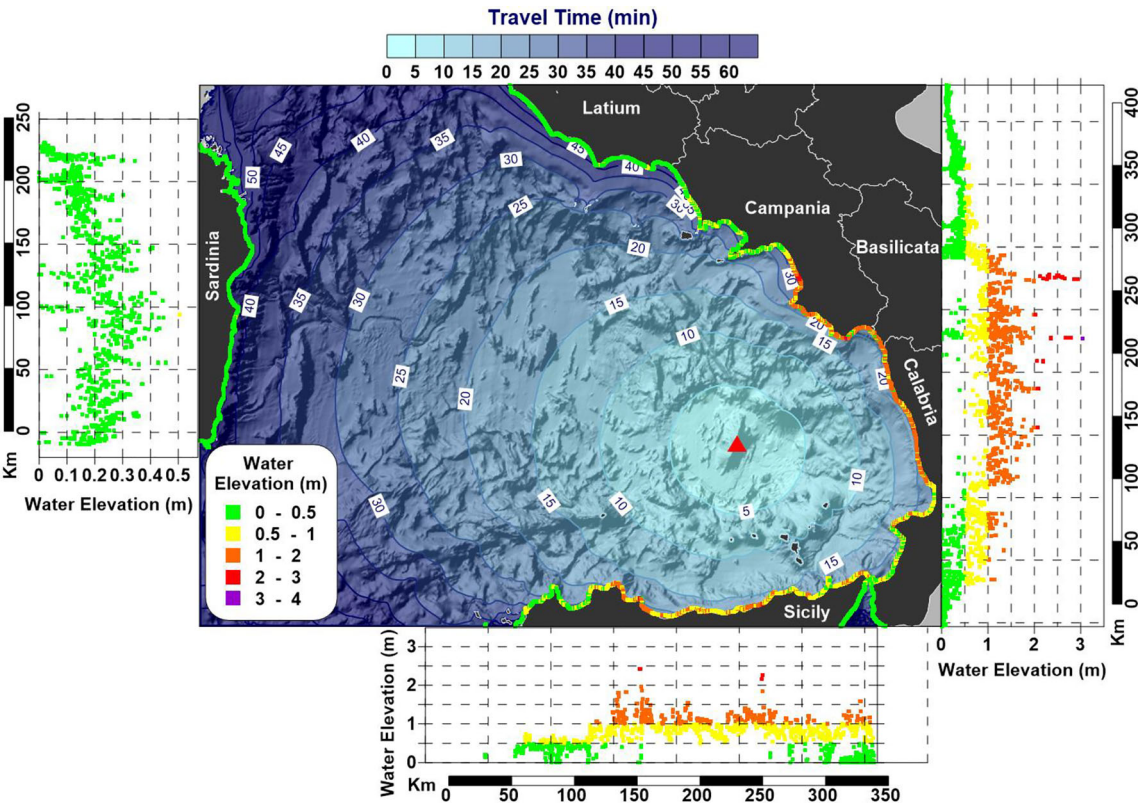

Fig. 13 Maximum water elevation along the coasts of the Tyrrhenian Sea, computed for the landslide case (e). See caption of Fig. 9 for details

have a similar origin and structure, although Vavilov is older than Marsili (Kastens et al. 1988), the future occurrence of large-scale gravity instability affecting the MS and generating the propagation of tsunami waves cannot be ruled out.

Cases (d) and (e), despite the different sliding volumes, show similar trajectory directions (Fig. 10), move quite rapidly with the same peak velocity for the center of mass (65 m/s), and produce similar tsunami propagation pattern and arrival times, but they correspond to different sea elevations (Figs. 12 and 13). This is not surprising since the propagation depends chiefly on the bathymetry, which is the same for all cases, while the size of the tsunami is correlated to the intensity of the initial forcing that, in turn, is related to the thickness and displacement of the related mass failure. This can give rise to an order of magnitude difference in the simulated tsunami waves.

It is remarkable to compare tsunami features of the reconstructed past case (c) and the hypothesized case (d), since they detach at similar depths, with comparable volumes (Table 1). The main difference lies in the location where the detachment occurs, respectively, in the north-western and south-eastern flanks of the volcanic edifice. As already observed above, the two scenarios share the initial radial propagation, but with reversed polarity: positive in the sliding direction (west for (c), east for (d), respectively), negative on the opposite side (see Fig. 8 and Fig. 11, upper panel). Apart from this, the two propagations are very similar: the coasts of Sicily and Calabria are affected by the waves 20 min after the slide onset. The maximum water elevations are quite similar for the two cases. However, a difference can be found along the coasts of Sardinia, where case (c) prevails (see Fig. 9 and Fig. 12). In Calabria, a negative-positive oscillation characterizes the first tsunami signal for case (c), while the opposite happens for case (d). In the former case, the first negative signal (Fig. 8), corresponding to a sea withdrawal, could be a key factor for early warning issues, while in the second circumstance (Fig. 11), no precursors of an incoming wave could be recognized. These considerations enhance the importance of further investigations, especially on the western slope of Marsili Seamount. As for the Sardinia coasts, the situation is reversed, but the estimated waves are smaller (0.5–1 m).

It is worth mentioning that, despite the magnitude of the simulated past failures, an area of maximum sea rise due to tsunamis (Fig. 7) is found over the MS crest, mainly depending on the bathymetry, and we could expect similar wave generation and/or propagation pattern for other mass failures hypothetically affecting other parts of the MS flank besides the hypothesized cases.

Of note is the difference between the computed strength of the fronts travelling eastward (that is, along the same direction as the landslide trajectory for case (d)) and westward (that is, in the opposite path, for case (c)). The eastward front is much stronger and therefore potentially more dangerous than the latter. Indeed, the elevations of the maximum simulated waves would hit the coasts of the Sicily and Calabria regions, while waves travelling in the opposite direction towards Sardinia have smaller (though still relevant) effects.

Portions of these coasts are vastly populated, especially during the summer months. Nowadays, the lack of a tsunami warning system for landslide-induced waves in Italy makes these kinds of phenomena more dangerous. Furthermore, the social perception of tsunami risk in this region (see Gravina et al. 2019) and in the whole Mediterranean basin is overall very low, due to the time interval elapsed since historical hazardous events. These aspects together enhance the tsunami risk for a large part of the above-mentioned coasts.

Finally, the worst-case scenario of failure of a 17.6-km^3 mass (case (e)) shows the generation of a potentially catastrophic tsunami, with waves as high as 20 m reaching the coasts of Calabria and Sicily regions in about 20 min. This hypothetical result must not be intended in a hazard perspective but serves to depict the possible consequence of large collapses on a seamount in the Tyrrhenian basin. Indeed, there are several other volcanic structures in the Tyrrhenian basin (see Rovere et al. 2016; Cocchi et al. 2017; see also the recent contribution by Gallotti et al. 2020 on tsunami potential from the Palinuro complex), and their nature and eruption history are still poorly known. Considering the well-known active volcanoes in the Aeolian archipelago, there is the need for intensifying studies to assess the overall hazard posed by these submarine and island volcanoes and, in particular, the hazard related to tsunami generation.

Conclusions

According to available studies on the Marsili Seamount (MS), the tsunamigenic potential of this submarine volcanic edifice, the largest in the Mediterranean Sea, is mostly related to gravity instability triggered by volcanic or seismic activity (Caratori Tontini et al. 2010). This study has demonstrated that (1) a relatively small-scale mass movement and a medium-size collapse in deep waters occurred on the MS flanks (Caratori Tontini et al. 2010; Ventura et al. 2013) should not have generated relevant tsunamis and (2) a medium-size collapse presumably detached from the volcano summit possibly induced a tsunami wave as high as 4 m in the surrounding coasts. Moreover, a worst-case scenario on the eastern flank shows that large-size failures detaching from the MS crest can generate waves as high as 20 m on the peri-Tyrrhenian coasts.

Our simulations confirm that the sliding volume is not the only factor controlling the size of the triggered tsunamis. The depth under the sea surface at which the movements occur plays a crucial role in the generation of the waves, while the propagation pattern is similar between different scenarios. Moreover, the outcomes of our study and of a recent parallel study on the neighboring Palinuro complex (Gallotti et al. 2020) suggest that the tsunami hazard related to these kinds of collapses should be further investigated in the Tyrrhenian sea.

Acknowledgments The authors wish to thank David R. Tappin and the other reviewers that are anonymous for their constructive and useful suggestions. The bathymetric data are available on the EMODNET web-portal. (http://www.emodnet.eu/). EMODnet Bathymetry Consortium (2018): EMODnet Digital Bathymetry (DTM). https://doi.org/10.12770/18ff0d48-b203-4a65-94a9-5fd8b0ec35f6.

Funding Open access funding provided by Alma Mater Studiorum - Università di Bologna within the CRUI-CARE Agreement.

References

Alves TM (2015) Submarine slide blocks and associated soft-sediment deformation in deep-water basins: a review. Mar Petrol Geol 67:262–285

Auker MR, Sparks RSJ, Siebert L, Crosweller HS, Ewert J (2013) A statistical analysis of the global historical volcanic fatalities record. J Appl Volcanol 2:2

Begét JE (2000) Volcanic tsunamis. In: Sigurdsson H, Houghton B, McNutt SR, Rymer H, Stix J (eds) Encyclopedia of volcanoes. Academic Press, New York, pp 1005–1013

Boudon G, Le Friant A, Komorowski JC, Deplus C, Semet MP (2007) Volcano flank instability in the Lesser Antilles Arc: diversity of scale, processes, and temporal recurrence. J Geophys Res 112: B08205. https://doi.org/10.1029/2006JB004674

Caratori Tontini F, Cocchi L, Muccini F, Carmisciano C, Marani M, Bonatti E, Ligi M, Boschi E (2010) Potential-field modelling of collapse-prone submarine volcanoes in the southern Tyrrhenian Sea (Italy). Geophys Res Lett 37:L03305. https://doi.org/10.1029/2009GL041

Cocchi L, Caratori Tontini F, Muccini F, Marani MP, Bortoluzzi G, Carmisciano C (2009) Chronology of the transition from a spreading ridge to an accretional seamount in the Marsili backarc basin (Tyrrhenian Sea). Terra Nova 21:369–374

Cocchi L, Passaro S, Caratori Tontini F, Ventura G (2017) Volcanism in slab tear faults is larger than in island-arcs and back-arcs. Nat Commun 8:1451. https://doi.org/10.1038/s41467-017-01626-w

D'Alessandro A, D'Anna G, Luzio D, Mangano G (2009) The INGV's new OBS/H: analysis of the signals recorded at the Marsili submarine volcano. J Volcanol Geotherm Res 183:17–29

Day SJ (2015) Chapter 58 – Volcanic tsunamis. In: Sigurdsson, Haraldur (Ed.), The encyclopedia of volcanoes, second edition. Academic Press, Amsterdam. ISBN9780123859389 pp.993–1009

Dutykh D, Dias F (2009) Tsunami generation by dynamic displacement of seabed due to dip-slip faulting. Math Comp Simul 80:837–848

EMODnet Bathymetry Consortium (2018) EMODnet Digital Bathymetry (DTM). https://doi.org/10.12770/18ff0d48-b203-4a65-94a9-5fd8b0ec35f6

Gallotti G, Passaro S, Armigliato A, Zaniboni F, Pagnoni G, Wang L, Sacchi M, Tinti S, Ligi M, Ventura G (2020) Potential mass movements on the Palinuro volcanic chain (southern Tyrrhenian Sea, Italy) and consequent tsunami generation. J Volcanol Geotherm Res 404:107025. https://doi.org/10.1016/j.jvolgeores.2020.107025

Giachetti T, Paris R, Kelfoun K, Ontowirjo B (2012) Tsunami hazard related to a flank collapse of Anak Krakatau Volcano, Sunda Strait, Indonesia. Geological Soc, London, Special Publications 361:79–90. https://doi.org/10.1144/SP361.7

Gravina T, Mari N, Farina L, Calabria P (2019) Tsunami risk perception along the Tyrrhenian coasts of Southern Italy: the case of Marsili volcano. Nat Hazards 97:437–454. https://doi.org/10.1007/s11069-019-03652-x

Grilli ST, Watts P (2005) Tsunami generation by submarine mass failure. In: Modeling, experimental validation, and sensitivity analyses. J Waterw Port C-Asce 131: 283–297

Grilli ST, Tappin DR, Carey S, Watt SFL, Ward SN, Grilli AR, Engwell SL, Zhang C, Kirby JT, Schambach L, Muin M (2019) Modelling of the tsunami from the December 22, 2018 lateral collapse of Anak Krakatau volcano in the Sunda Straits, Indonesia. Sci Rep 9:11946. https://doi.org/10.1038/s41598-019-48327-6

Harbitz CB (1992) Model simulations of tsunamis generated by the Storegga slides. Mar Geol 105:1–21

Harbitz CB, Løvholt F, Pedersen G, Masson DG (2006) Mechanisms of tsunami generation by submarine landslides: a short review. Nor J Geol 86:255–264

Homa JL (2009) Timing of occurrence of large submarine landslides on the Atlantic Ocean margin. Mar Geol 264:53–64

Hunt JE, Cassidy M, Talling PJ (2018) Multi-stage volcanic island flank collapses with coeval explosive caldera-forming eruptions. Sci Rep 8:1146

Iezzi G, Caso C, Ventura G, Vallefuoco M, Cavallo A, Behrens H, Mollo S, Paltrinieri D, Signanini P, Veterea F (2014) First documented deep submarine explosive eruptions at the Marsili Seamount (Tyrrhenian Sea). Gondwana Res 25:764–774. https://doi.org/10.1016/j.gr.2013.11.001

Karstens J, Berndt C, Urlaub M, Watt SFL, Micallef A, Ray M, Klaucke I, Muff S, Klaeschen D, Kühn M, Roth T, Böttner C, Schramm B, Elger J, Brune S (2019) From gradual spreading to catastrophic collapse – reconstruction of the 1888 Ritter Island volcanic sector collapse from high-resolution 3D seismic data. Earth Planet. Sci Lett 517: 1–13

Kastens K, Mascle J, Auroux C, Bonatti E, Broglia C., Channell J, Curzi P, Emeis KC, Glacon G, Hasegawa S, Hieke W, Mascle G, McCoy F, McKenzie J, Mendelson J, Muller C, Rehault JP, Robertson A, Sartori R, Sprovieri R, Torii M (1988) ODP Leg 107 in the Tyrrhenian Sea: insights into passive margin and back-arc basin evolution. Geol. Soc Amer Bull 100: 1140–1156

Ligi M, Cocchi L, Bortoluzzi G, D'Oriano F, Muccini F, Caratori Tontini F, de Ronde CEJ, Carmisciano C (2014) Mapping of seafloor hydrothermally altered rocks using geophysical methods: Marsili and Palinuro seamounts, southern Tyrrhenian Sea. Econ Geol 109:2103–2117

Lo Iacono C, Gràcia E, Zaniboni F, Pagnoni G, Tinti S, Bartolomé R, Masson DG, Wynn RB, Lourenço N, Pinto de Abreu M, Dañobeitia JJ, Zitellini N (2012) Large, deepwater slope failures: implications for landslide-generated tsunamis. Geology 40:931–934. https://doi.org/10.1130/G334461

Locat J, Lee HJ (2002) Submarine landslides: advances and challenges. Can Geotech J 39:193–212

Loughlin SC, Luckett R, Ryan G, Christopher T, Hards V, De Angelis S, Jones L, Strutt M (2010) An overview of lava dome evolution, dome collapse and cyclicity at Soufrière Hills Volcano, Montserrat, 2005–2007. Geophys Res Letters 37:1–6. https://doi.org/10.1029/2010GL042547

Løvholt F, Pedersen G, Harbitz CB, Glimsdal S, Kim J (2015) On the characteristics of landslide tsunamis. Philosophical Transactions of the Royal Society A 373: 20140376.

Marani M (2004) Super-inflation of a spreading ridge through vertical accretion in the Tyrrhenian Sea: the arc vs the backarc. Memorie Descrittive della Carta Geologica d'Italia 44:109–126

Marani M, Trua T (2002) Thermal constriction and slab tearing at the origin of a superinflated spreading ridge: the Marsili volcano

(Tyrrhenian Sea). J Geophys Res 107:2188–EPM 3-15. https://doi.org/10.1029/2001JB000285

McGuire WJ (1996) Volcano instability: a review of contemporary themes. Geol Soc, London, Special Publications 110: 1–23 110(1 January 1996):1–23. https://doi.org/10.1144/GSL.SP.1996.110.01.01

Pagnoni G, Armigliato A, Tinti S (2015) Scenario-based assessment of buildings' damage and population exposure due to earthquake-induced tsunamis for the town of Alexandria, Egypt. Nat Hazards Earth Syst Sci 15: 2669–2695. https://doi.org/10.5194/nhess-15-2669-2015

Paparo MA, Tinti S (2017) Analysis of seismic-driven instability of Mt. Nuovo in the Ischia Island, Italy. Bull Seismol Soc Am 107:750–759. https://doi.org/10.1785/0120160139

Pelinovsky E, Poplavsky A (1996) Simplified model of tsunami generation by submarine landslides. Phys Chem Earth 21:13–17

Reid ME (2004) Massive collapse of volcano edifices triggered by hydrothermal pressurization. Geology 32:373–376. https://doi.org/10.1130/G20300.1

Rovere M, Bo M, Alessi J, Paoli C, Villani N, Vassallo P, Fiori C, Roccatagliata N (2016) Seamounts and seamount-like structures of the Tyrrhenian Sea. In: Atlas of the Mediterranean seamounts and seamount-like structures. Publisher: IUCN, Gland, Switzerland and Málaga, Spain. Editors: Maurizio Würtz, Marzia Rovere, pp.111–184

Sadourny R (1975) The dynamics of finite-difference models of the shallow-water equations. J Atmos Sci 32:680–689. https://doi.org/10.1175/1520-0469(1975)032<0680:TDOFDM>2.0.CO;2

Satake K (2001) Tsunami modelling from submarine landslides. Proc Intern Tsunami Symp

Siebert L, Glicken H, Ui T (1987) Volcanic hazards from Bezymianny- and Bandai-type eruptions. Bull Volcanol 49:435–459

Synolakis SE (2003) Tsunami and seiche. Earthquake eng. Handbook, Publisher: CRC Press, Boca Raton, FL, USA. Editors: Wai-Fah Chen, Charles Scawthorn, pp. 9_1–9_79

Tamburrino S, Vallefuoco M, Ventura G, Insinga DD, Sprovieri M, Tiepolo M, Passaro S (2015) The proximal marine record of the Marsili Seamount in the last 7 ka (Southern Tyrrhenian Sea, Italy): implications for the active processes in the Tyrrhenian Sea back-arc. Glob Planet Change 133:2–16

Tinti S, Piatanesi A (1997) Finite-element simulations of the 5 February 1783 Calabrian tsunami. Phys Chem Earth 12:39–43

Tinti S, Tonini R (2013) The UBO-TSUFD tsunami inundation model: validation and application to a tsunami case study focused on the city of Catania. Italy Nat Hazards Earth Syst Sci 13:1795–1816. https://doi.org/10.5194/nhess-13-1795-2013

Tinti S, Bortolucci E, Vannini C (1997) A block-based theoretical model suited to gravitational sliding. Nat Hazards 16:1–28

Tinti S, Bortolucci E, Armigliato A (1999) Numerical simulation of the landslide-induced tsunami of 1988 on Vulcano Island, Italy. Bull Volcanol 61:121–137

Tinti S, Pagnoni G, Zaniboni F (2006) The landslides and tsunamis of the 30th of December 2002 in Stromboli analysed through numerical simulations. Bull Volcanol 68:462–479

Trua T, Serri G, Renzulli A, Marani MP, Gamberi F (2002) Volcanological and petrological evolution of Marsili seamount (southern Tyrrhenian Sea). J Volcanol Geotherm Res 114:441–464

Trua T, Marani MP, Gamberi F (2018) Magma plumbing system at a young back-arc spreading center: the Marsili Volcano, Southern Tyrrhenian Sea. Geochem Geophys Geosyst 19:43–59. https://doi.org/10.1002/2017GC007151

Vanneste M, Mienert J, Bünz S (2006) The Hinlopen Slide: a giant, submarine slope failure on the northern Svalbard margin, Arctic Ocean. Earth Planet Sc Lett 245:373–388

Ventura G, Milano G, Passaro S, Sprovieri M (2013) The Marsili Ridge (Southern Tyrrhenian Sea, Italy): an island-arc volcanic complex emplaced on a 'relict' back-arc basin. Earth-Science Rev 116: –8594

Ward SN (2001) Landslide tsunami. J Geophys Res 106:11201–11215

Ward SN, Day S (2001) Cumbre Vieja Volcano - potential collapse and tsunami at La Palma, Canary Islands. Geophys Res Lett 28:3397–3400

Watt S, Talling PJ, Hunt JE (2014) New insights into the emplacement dynamics of volcanic island landslides. Oceanography 27:46–57

Waythomas CF, Watts P, Shi F, Kirby JT (2009) Pacific Basin tsunami hazards associated with mass flows in the Aleutian arc of Alaska. Quat Sci Rev 28:1006–1019

Zaniboni F, Tinti S (2019) The 1963 Vajont landslide: a numerical investigation on the sliding surface heterogeneity. Pure Appl Geophys 176:279–295. https://doi.org/10.1007/s00024-018-2023-6

Zaniboni F, Pagnoni G, Tinti S, Della Seta M, Fredi P, Marotta E, Orsi G (2013) The potential failure of Monte Nuovo at Ischia Island (Southern Italy): numerical assessment of a likely induced tsunami and its effects on a densely inhabited area. Bull Volcanol 75:763. https://doi.org/10.1007/s00445-013-0763-9

Zaniboni F, Armigliato A, Pagnoni G, Tinti S (2014) Continental margins as a source of tsunami hazard: the 1977 Gioia Tauro (Italy) landslide-tsunami investigated through numerical modelling. Mar Geol 357:210–217

Zaniboni F, Armigliato A, Tinti S (2016) A numerical investigation of the 1783 landslide-induced catastrophic tsunami in Scilla, Italy. Nat Hazards 82:455–470